

1 **Geochemical characteristics of hydrothermal manganese deposits in the**

2 **Sulaimani metallogenic district, Kurdistan Region of Iraq: A**

3 **serpentinization marker**

4 **Abstract**

5 This research investigates the geochemical characteristics of hydrothermal manganese deposits
6 in the Sulaimani metallogenic district, Kurdistan Region of Iraq, to understand their formation
7 processes, which may aid in the exploration of manganese resources in the region. These
8 deposits are intimately associated with various units of Mesozoic Qulqula Formation, including
9 jasperite, umber, radiolarian chert, siliceous shale, brown claystone, and basalt sequences of
10 the Penjween ophiolite in the Mlakawa - Tapa sura area. In the Sulaimani district, two types of
11 manganese deposits are found: strata-bound deposits with a thickness of around 200 meters,
12 interbedded with late Cretaceous eip-ophilitic radiolarite chert of the Penjween ophiolite
13 complex, and as exotic massive bodies within Eocene Merga Group, forming boulder placer
14 deposits. The manganese deposits exhibit geochemical characteristics such as intermediate
15 MnO content (up to 24 wt.%), low levels of transitional elements ($\text{Co} + \text{Ni} + \text{Cu} < 0.01 \text{ wt.}\%$),
16 elevated concentrations of Ba (up to 4490 ppm), and low total rare earth elements. Geochemical
17 analyses reveal negative Ce anomalies (-0.016 _ -1.024) and positive Y anomalies (3.4 _ 22.3)
18 in most samples, indicative of submarine hydrothermal processes within the Neotethys.
19 However, some banded-type deposits show weak positive Ce anomalies (0.1), suggesting
20 minor diagenetic influences. The presence of weak negative Eu anomalies (0.54 _ 0.71) in all
21 samples likely reflects the low Eu content in the ultramafic parent rocks and the influence of
22 low-temperature hydrothermal serpentinization fluids. In summary, the geochemical signatures
23 suggest that these manganese deposits, associated with regional radiolarite facies within the
24 Neotethys, originate from mid-oceanic ridge proximal to distal hydrothermal sources.

25

26 **Keywords:** *Manganese deposits, Neotethys, Banded chert, Zagros orogeny, Sulaimani*

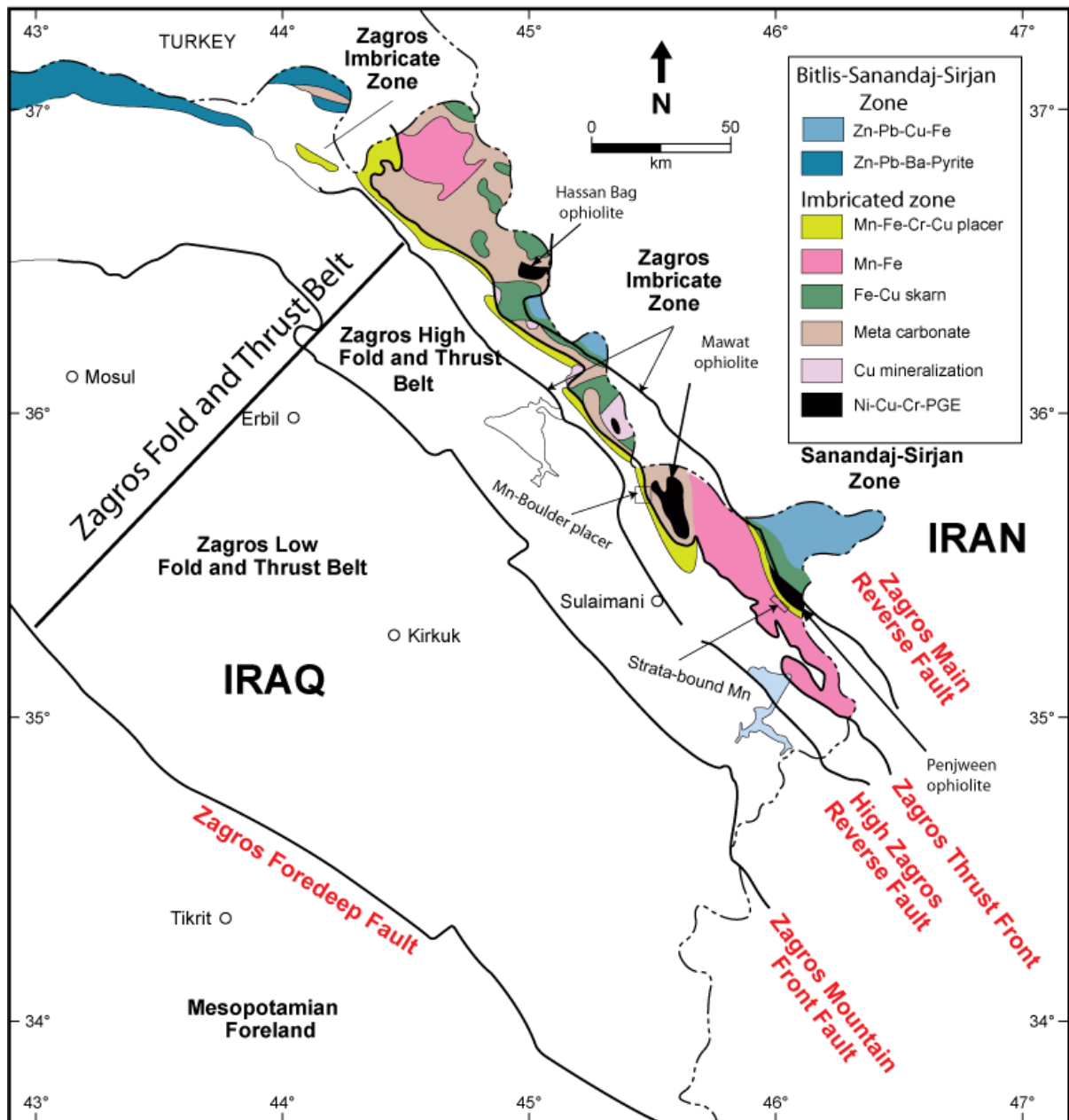
27

28 **1. Introduction**

29 The significant and extensive Zagros Mountain belt in the Kurdistan region of Iraq emerged
30 from the continental break off the Sanandaj–Sirjan Zone (SaSZ) from the North west of Afro-
31 Arabian plate margin and the subsequent accretion of Eurasia (Jassim and Goff 2006). This
32 was followed by Eocene amalgamation with Arabian plate (Mohammad et al. 2020, Nutman
33 et al. 2022). The time sequence of the tectonic evolution of Zagros collisional orogens typically
34 involves three major **tectonic events**: (1) Permian crustal divergence, (2) Late Cretaceous
35 convergence, and (3) Eocene collisional, each giving rise to distinct types of ore deposits in
36 specific time and **diverse** geological settings. The timing and distribution of mineral deposits
37 in various region of Iraq demonstrate a strong correlation with tectonic divisions. **In the**
38 **Kurdistan region of Iraq, significant mineral deposits are characterized by endogenic metallic**
39 **mineralization from the Jurassic, Upper Cretaceous, and Paleogene periods. These are**
40 **connected to hydrothermal, magmatic, sedimentary, and metamorphic processes associated**
41 **with regional orogenic phases** (Al-Bassam 2013).

42 The Kurdistan region of Iraq can be divided into two main metallogenic zones based on the
43 regional tectonic framework of the Zagros orogenic belt. These zones are the Imbricate Zone
44 of the Western Zagros Fold-Thrust Belt and the Bitlis-Sanandaj-Sirjan Zone (Fig 1; compiled
45 from Al-Bassam 1984, Jassim and Goff 2006, Fouad 2012, Mohammad et al. 2014, Al-Bassam
46 2013). The former zone encompasses three mineral belts i) Qulqula-Khwakurk Mn-Fe belt is
47 composed of hydrothermal and diagenetic Mn-Fe deposits within the radiolarian chert of the
48 Early Cretaceous part of the Qulqula Series; ii) Penjween-Walash Cr, Ni, Cu, Fe belt, it

49 contains orthomagmatic Cr, Ni, Fe, Cu and contact metasomatic skarn Fe. This belt consists of
 50 the Qandil Series (Early Cretaceous), basic and ultrabasic Igneous ophiolite Complexes (Late
 51 Cretaceous), and volcano sedimentary units of Walash and Naopurdan Groups (Tertiary); iii)
 52 Tertiary Red Beds placer deposit belt of Mn and Fe (Buday and Jassim 1984, Jassim and Guff
 53 2006, Al-Bassam 2013, Sissakian 2018).



54

55 Fig 1. Tectono- mineralogic map of Kurdistan region of Iraq, showing various mineral deposits belts
 56 superimposed on major tectonic zones (Tectonic subdivision from Mohammad et al. 2014).

57 Conversely, the Bitlis-Sanandaj-Sirjan Zone (BSaSZ) exhibits a diverse array of ore deposits
58 that were formed during the Mesozoic era, including orthomagmatic, metamorphic, and
59 hydrothermal deposits. Within the BSaSZ of Iraq, there are two significant metallogenic belts
60 known as the i) Shalair -Marabasta Zn, Pb, Fe belt in the southeast. This belt is characterized
61 by Jurassic metamorphosed Zn, Pb, and pyrite strata-bound deposits, which occur in carbonate
62 rocks of Triassic origin. ii) The Ora belt in the north west, which includes both low temperature
63 hydrothermal Ba, Cu, Pb, Zn, and pyrite veins, as well as to Late Triassic -Late Cretaceous
64 syngenetic strata-bound deposits of Zn and Pb, along with disseminated pyrite in massive
65 carbonate rocks; Additionally, there are other deposits found in the region, such as Fe and Zn
66 skarns, volcanogenic Cu and Fe mineralizations, and Cretaceous marble deposits.

67 Manganese deposits are known to come from various sources, characterized by differences in
68 mineralogy, chemical composition, and tectonic context (Polgari et al., 2012). Marine
69 manganese deposits are categorized as hydrogenous, diagenetic, hydrothermal, or biogenetic-
70 bacterial (Oksuz 2011, Polgari et al. 2012). Furthermore, Mosier and Page (1988) identified
71 four types of manganese deposits based on their tectonic settings: Franciscan, Cuban, Olympic
72 Peninsula, and Cyprus types.

73 The Zagros hydrothermal manganese and ferromanganese deposits are commonly associated
74 with fragments of the Neotethys oceanic crust, which include radiolarian cherts and basaltic
75 rocks forming the top crustal unit ophiolite sequences (Zarasvandi 2016, Maghfouri et al.
76 2019, Aydoğan, 2021). The upper pelagic sedimentary facies of the Neotethys oceanic basin
77 extended from southern Oman, through western Iran's Kermanshah region, passing by Qulqula
78 in the Kurdistan region of Iraq, and ending with the Kocali basin in northern Turkey (De Wever
79 et al. 1988, Mohammad and Qaradaghi 2016). Many economically significant manganese and
80 ferromanganese deposits have been documented in various locations in association with
81 Neotethys radiolarite, such as Oman (Al Hammah Range - Wahrah Formation), Iran

82 (Nasirabad and Abadeh, Gugher and Gushk, Tashk, Sorkhvand and Kamyaran deposits),
83 Turkey Emir deposit (Sorgun-Yozgat deposit), Greece (Andros), and Cyprus (Troodos Massif)
84 (Kickmaier and Peters 1990, Öztürk 1997, Maghfouri et al. 2019).

85 Manganese occurrences connected to the Qulqula-Khwakurk Mn-Fe belt in the Kurdistan
86 region of Iraq have been recorded (Latif et al. 2022 and references therein). However, specific
87 geochemical signatures of the manganese deposits associated with the **Neotethys** ophiolite unit
88 in the Kurdistan region of the Zagros orogeny have not been considered. Consequently, this
89 study marks the first effort to precisely describe these deposits, conduct comprehensive
90 geochemical investigations, and explore the geological settings of manganese occurrences in
91 this region. Furthermore, utilizing available geochemical datasets of manganese deposits across
92 the region, we propose a geodynamic model that may elucidate the origin of Neotethys
93 manganese and ferromanganese in radiolarite chert.

94 **2. Geological setting and mode of occurrences of manganese deposits**

95 Narrow belts and sporadic units of manganese deposits are found within radiolarian chert and
96 Red Bed series in the Imbricated Zone of the Kurdistan region in Iraq (Fig 1). These deposits
97 are situated in a continuous belt that stretches across the Sulaimani metallogenic province,
98 running from the southeast to the **northwest** along the collision zone. The manganese deposits
99 in the epi-ophiolitic rock are closely associated with jasperite, umber (**Fig.2**), radiolarian chert,
100 siliceous shale, brown claystone, and a basalt succession of Penjween ophiolite in the Mlakawa
101 - Tapa sura area.

102 The chert sequences in the area mainly represent the bedded facies of Qulqula radiolarite,
103 which were deposited during the middle Jurassic to early Late Cretaceous period in the
104 **Neotethys** oceanic basin (Baziany 2014). Most manganese mineralization is typically found
105 in close proximity to reddish-brown radiolarian cherts that overlie the volcanic unit of the

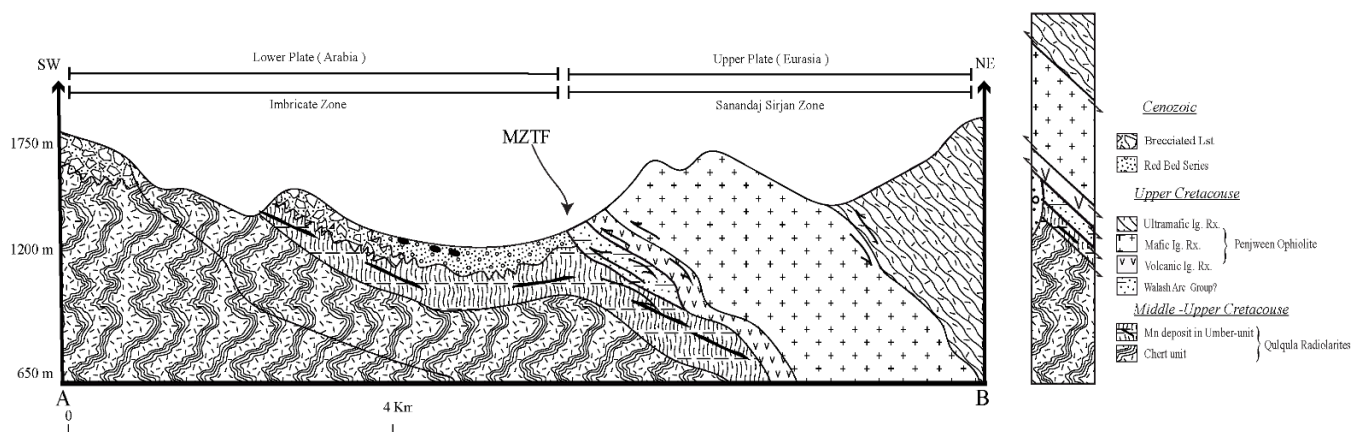
106 Penjween ophiolite during the deposition process before final thrusting and emplacement
107 stages of the Neotethys oceanic basin in the form of fossil fragment ophiolite (Fig.2).

108 Penjween ophiolite consists of about 300 m thick mantle sequences mostly serpentized
109 harzburgite with some restricted dunite, pyroxenite veins and chromitite pods to the southwest,
110 occupying the summit of Mlakawa mountain, to the west followed by about 2 Km crustal
111 sequences represent by various types of gabbro, dykes of diorite and volcanic rocks at the
112 Mlakawa mountain slope and base respectively (Mohammad et al. 2007, Mohammad, 2011,
113 Mohammad et al. 2021). Within the volcanic units occasionally bolder and patches of
114 metalliferous recrystallized quartz dominated rock occurs north of the Kani Manga village. The
115 volcanic unit is underlined by umber unit then followed by typical chert unit of Qulqula
116 Formation. As a result of the intense deformation, squeezing and extensive thrusting a
117 combined obduction-collision events in the area it is obvious that the stratigraphy sequence of
118 the Penjween ophiolite complex apparently overturned (Fig.2). Field investigations have
119 revealed the presence of various ore structures and sizes associated with radiolarian cherts,
120 including layered, vein (2-5 cm thick veins), macronodular (1-3 cm across), and banded
121 manganese (0.1 to 0.2 thick mm band) mineralization located approximately 5 kilometers
122 southwest of Penjween ophiolite.

123 **3. Mineralogy and Mineral paragenetic**

124 Latif et al., 2022 based on detail ore microscopic investigations and XRD phase identifications
125 confirmed that the mineralogy of manganese deposits in Sulaimani metallogenic province are
126 relatively simple. The ore consists mainly of pyrolusite dominated with minor hollandite for
127 the banded, vein and layer types of the ore, while massive types are braunite and rhodonite
128 dominated. Quartz, cryptocrystalline silica, calcite, iron oxides and clay minerals are gangue
129 minerals. Through sequences of layers in vein filling, replacement relationships among the

130 manganese phases, recrystallization and deposition relative to the distal and proximal area of
 131 the discharging sources and subsequent metamorphism. Thus, it is evidenced from these
 132 relationships that the manganese deposit in the area may have formed through four successive
 133 stages as follow: Hydrothermal → Nano manganese deposition → Diagenetic → Metamorphic
 134 stages. Detail of mineralogy and paragenetic sequence described in Latif et al. 2022.



135
 136 **Figure 2: Geological cross section and stratigraphic column of Penjween area, showing the main**
 137 **lithostratigraphic units in addition to manganese occurrence.**

138
 139 **4. Analytical methods**

140 14 samples representing diverse manganese occurrences in the Sulaimani Metallogenic
 141 provinces, have been selected for geochemical investigation through laboratory-based
 142 examination. The numbers of samples from manganese deposits chosen for geochemical
 143 analysis are illustrated in Table 1. These include 3 samples from the massive type, 4 samples
 144 from the vein type, 5 samples from another vein type, and 2 samples from the host rock.
 145 Laboratory-based investigations included routine polarized transmitted-incident optical
 146 microscopy, complemented by Scanning Electron Microscope (SEM) and X-ray diffraction
 147 (XRD) studies. The microscopic examinations and XRD analysis were conducted at the
 148 Geology department of Sulaimani University, Kurdistan Region of Iraq. Detail results of
 149 mineral components and mineralogical description can be seen in Latif et al. 2022.

150 The analysis for major, trace elements, and Rare Earth Elements (REE) in the whole-rock
151 samples was carried at a certified lab (ALS Laboratory Group, SL), using ICP-AES with the
152 Lithium Borate fusion method as part of the whole-rock package encoding ME-MS81d and
153 ME-4ACD81. The QC/QA process involved analyzing duplicate samples (7% of the total
154 samples), blanks, and certified reference materials (EMOG-17, MRGeo08). The concentration
155 of major, trace, and REE in the samples given in tables 1 and 2. Additionally, the correlation
156 coefficients between various oxides, trace elements, and REEs can be found in Appendix 1.

157 In this study, the RQ-mode PCA (Principal Component Analysis) method is used (Neff, 1994),
158 which aids in conducting a more insightful analysis of the relationships between variables
159 (elements) and observations (samples). By employing RQ-mode PCA, we can effectively
160 examine and understand the interrelationships among variables and observations for the
161 available geochemical dataset of manganese deposit in the study area. This approach may lead
162 to a deeper understanding of the geochemical characteristics of the manganese deposit and
163 allows for the exploration of element associations, providing valuable insights into the
164 geological processes and factors influencing the deposit's formation.

165 **4. Results**

166 The SiO₂ concentration varies from 63.6 to 96.3 wt.%, with an average of 77.25 wt. %, and
167 CaO from 0.07 to 4.76 wt. %, with an average of 1.12 wt. % (Table 1). The samples have a low
168 Al₂O₃ content, ranging from 0.54% to 2.55% by weight, with an average of 1.39%. X-ray
169 diffraction analysis reveals a significant presence of clay, primarily in the form of
170 montmorillonite (Latif et al. 2022). The total alkali content in the samples is remarkably low,
171 ranging from 0.03% to 0.98% by weight. The analyzed samples exhibit a low MgO content,
172 varying from 0.06% to 0.46% by weight, with an average of 0.27%. The samples exhibit high
173 Fe₂O₃ content, ranging from 0.5% to 15% by weight, with an average of 4.29%. The maximum

174 Fe₂O₃ concentrations are found in the massive types of manganese deposits and jasperite. The
175 analyzed samples from the Sulaimani **metallogenic** province display a wide range of MnO
176 content, varying from 4.9% to 23.9 % by weight, with an average of 11.52%. -Notably, higher
177 concentrations of MnO have been found in the vein types of deposits, with the maximum
178 reaching 24 % and the lowest in the metalliferous Umber unit. The concentration of TiO₂ in all
179 samples is relatively low, with values less than 0.5% by weight, and in some cases, it is even
180 less than 0.01%. The concentration of P₂O₅ in all samples is relatively low, being less than
181 0.12% by weight. The concentration of BaO in the samples is relatively low but higher
182 compared to other oxides like P₂O₅ and TiO₂, ranging from 0.1% to 1.09% by weight. The
183 highest concentration of BaO is recorded in the massive types of manganese deposits. This
184 high concentration indicates the presence of mineral **barite** in the massive deposits, which
185 reflects a substantial contribution of oceanic water to the formation of these deposits. In the
186 manganese deposit samples, the compatible trace elements comprise Ni, Co, Cr, V, and Cu.
187 The concentrations of these elements vary in different types of manganese mineralization
188 within the studied area. The highest values of Cr and Co are recorded in vein types of
189 manganese deposits, while the highest concentrations of Ni, Zn, and V are found in massive
190 types. In the studied area, the concentrations of **Large-Ion lithophile element** (LILE) vary
191 across different types of manganese deposits. The highest values of LILEs are recorded in veins
192 and banded types of manganese deposits, while the lowest concentrations are found in massive
193 types.

194 In the studied samples **High field strength elements** (HFSE) include Ti⁴⁺, Zr⁴⁺, Nb⁵⁺, Ta⁵⁺, and
195 Hf⁴⁺. The concentration behavior of HFSE relative to LILEs is exactly opposite, with the
196 highest HFSE concentrations.

197 Table 1. ICP-MS results of the major and trace element composition from various types of manganese deposits in the Sulaimani metallogenic
 198 province.

Sample No.	DY-1	DY-2	DY-3	DY-4	DY-5	DY-6	DY-7	DY-8	DY-9	DY-10	DY-11	DY-14	DY-12	DY-13
Major oxides (wt. %)	Massive type			Chert	Vein type				Banded type					Jasperite
Latitude (N)	35° 54' 49"			35° 30' 00"	35° 29' 59"				35° 30' 41"					35° 30' 00"
Longitude (E)	45° 23' 82"			45° 57' 87"	45° 58' 01"				45° 57' 49"					45° 57' 87"
SiO ₂	63.6	68.3	65.6	96.3	69.7	79.3	64.6	71.7	83.5	77.7	76.6	86.8	86.7	91.1
Al ₂ O ₃	0.54	0.31	0.55	0.76	1.23	1.14	1.9	1.8	2.34	2.4	1.78	2.55	0.09	0.49
TiO ₂	0.03	0.01	0.03	0.03	0.06	0.05	0.11	0.1	0.13	0.14	0.11	0.14	0.01	<0.01
MgO	0.27	0.16	0.34	0.06	0.26	0.19	0.43	0.46	0.33	0.33	0.19	0.45	0.06	0.28
Fe ₂ O ₃	14.2	15.9	8.64	0.53	0.91	0.59	1.03	1.08	1.5	1.35	1.16	1.4	4.01	7.83
CaO	3.63	2.69	4.76	0.7	1.6	0.21	0.52	0.49	0.25	0.23	0.16	0.39	0.07	0.05
Na ₂ O	0.04	0.02	0.02	0.13	0.1	0.13	0.16	0.15	0.12	0.11	0.11	0.12	0.03	0.02
K ₂ O	0.02	0.01	0.01	0.14	0.17	0.42	0.76	0.83	0.4	0.38	0.25	0.49	0.03	0.02
MnO	13	8.54	18.7	0.09	20.2	12.85	23.9	18.85	7.42	12.65	14.15	4.92	5.9	0.06
P ₂ O ₅	0.08	0.05	0.1	0.06	0.07	0.04	0.09	0.07	0.03	0.04	0.02	0.12	0.03	0.03
SrO	0.01	0.01	0.01	0.01	0.01	0.02	0.02	0.02	0.01	<0.01	0.01	<0.01	0.01	<0.01
BaO	0.25	0.15	0.42	0.021	0.82	0.54	1.097	0.885	0.14	0.231	0.202	0.178	0.1	0.1
LOI	2.48	2.1	2.68	1.71	5.69	3.37	5.78	4.87	3.82	4.53	4.29	3.54	1.95	0.46
Trace elements (ppm)														
As	67	44	43	<5	8	<5	7	7	<5	<5	5	<5	48	6
Cr	20	20	10	40	20	50	70	60	10	10	10	20	20	30
Co	9	7	21	2	60	23	39	37	51	68	36	61	1	1
Ni	139	92	218	7	51	12	28	26	32	41	31	82	236	1

Cu	102	60	187	12	715	505	1030	822	57	122	135	35	22	7
Sc	1	<1	1	1	3	2	3	3	4	4	3	4	<1	<1
Zn	115	75	165	4	43	22	41	36	23	32	25	28	172	28
Sr	71.5	32.3	33.8	27.4	81.1	162	244	245	75.9	73.4	100	44.7	45.4	3.6
Ba	673	577	1355	178.5	635	2900	4210	4490	279	391	452	550	2000	8.6
Y	10.6	6.3	12	12.1	10.9	3.5	8.2	6.2	3.4	4.6	4.8	22.3	4.5	5.7
Zr	10	4	11	11	28	15	24	21	27	27	21	25	27	3
U	1.01	0.53	1.28	0.18	2.03	2.89	2.58	2.31	0.81	1.22	1.41	0.45	0.42	0.06
V	335	219	297	6	130	110	180	171	26	38	44	23	66	23
Hf	0.2	<0.1	0.2	0.3	0.4	0.3	0.5	0.5	0.6	0.6	0.5	0.6	0.1	0.1
Pb	26	18	33	5	96	24	36	29	19	25	23	11	11	7
Li	10	10	<10	20	20	20	20	20	20	20	20	30	<10	<10
Nb	0.6	0.2	0.6	0.8	2.8	2	3.1	2.9	2.5	3.3	2.3	0.3	0.1	2.9
Cs	0.01	0.01	0.01	0.14	0.32	0.22	0.46	0.43	0.62	0.71	0.44	0.02	0.02	0.72
Ta	<0.1	<0.1	<0.1	<0.1	<0.1	<0.1	0.1	<0.1	0.1	0.1	<0.1	<0.1	<0.1	0.1
Tb	0.2	0.09	0.22	0.35	0.23	0.09	0.21	0.15	0.09	0.15	0.11	0.06	0.14	0.56
Th	0.42	0.09	0.43	0.62	0.74	0.56	1.13	0.96	1.29	1.35	0.98	<0.05	<0.05	1.31
Rb	0.7	0.4	0.3	2.9	5.2	4.6	9.2	9	13.1	12.7	8.1	0.4	0.3	14.7
Hf	0.2	<0.1	0.2	0.3	0.4	0.3	0.5	0.5	0.6	0.6	0.5	0.1	0.1	0.6
Ga	8	5.3	11.7	1.5	11.4	8.1	13.5	10.6	6.3	8.6	8.8	3.4	2	5.5
W	1	1	1	<1	8	31	<1	<1	9	18	24	8	2	1
Cu+Co+Ni	250	159	426	21	826	540	1097	885	140	231	202	178	259	9
(Cu+Co+Ni) *10	2500	1590	4260	210	8260	5400	10970	8850	1400	2310	2020	1780	2590	90
Co/Zn	0.08	0.09	0.13	0.5	1.4	1.05	0.95	1.03	2.22	2.13	1.44	2.18	0.01	0.04
Mn/Fe	1.02	0.59	2.4	0.19	24.5	24.12	25.69	19.33	5.48	10.38	13.51	3.89	1.63	0.01
Th/U	0.42	0.17	0.34	3.44	0.36	0.19	0.44	0.42	1.59	1.11	0.7	0	0	2.91
Co/Ni	0.06	0.08	0.1	0.29	1.18	1.92	1.39	1.42	1.59	1.66	1.16	0	0	0.74

200

201 Table 2. ICP-MS results of the Rare Earth Element (REE) geochemical composition from various types of manganese deposits in the Sulaimani
 202 metallogenic province. * After Taylor and MacLennan, 1985

Sample No.	DY-1	DY-2	DY-3	DY-4	DY-5	DY-6	DY-7	DY-8	DY-9	DY-10	DY-11	DY-14	DY-12	DY-13
REEs (ppm)	Massive types			Chert	Vein type				Banded type				Jasperite	
La	6.7	3.4	9.2	10.1	14.6	4.3	9.5	7.1	4.2	5.9	3.7	21.2	2.1	0.7
Ce	3.6	1.4	3.5	12.2	15.5	8.5	16.9	12.7	11.7	16.5	10.9	20.3	0.4	1.9
Pr	1.28	0.54	1.73	2.82	2.14	0.84	1.85	1.4	0.9	1.4	0.99	4.67	0.34	0.32
Nd	5.2	2.1	7	11.4	7.6	3	6.9	5.1	3.1	5.1	3.7	18.8	1.3	1.8
Sm	1.13	0.41	1.34	2.43	1.5	0.6	1.43	1.04	0.65	1.07	0.81	3.68	0.32	0.55
Eu	0.27	0.11	0.35	0.57	0.37	0.14	0.32	0.22	0.14	0.26	0.18	0.91	0.06	0.12
Gd	1.33	0.56	1.59	2.58	1.68	0.6	1.36	1.11	0.6	0.99	0.78	4.14	0.36	0.84
Dy	1.32	0.67	1.47	2.02	1.58	0.54	1.23	0.97	0.58	0.85	0.64	3.19	0.37	0.94
Ho	0.3	0.16	0.32	0.39	0.34	0.11	0.24	0.19	0.11	0.16	0.13	0.63	0.09	0.2
Er	0.91	0.52	0.96	1.01	1.12	0.31	0.74	0.58	0.34	0.46	0.39	1.76	0.34	0.66
Tm	0.1	0.05	0.1	0.12	0.13	0.04	0.09	0.07	0.04	0.06	0.04	0.19	0.04	0.08
Yb	0.69	0.41	0.64	0.77	1.07	0.29	0.64	0.51	0.35	0.45	0.33	1.18	0.27	0.53
Lu	0.1	0.06	0.1	0.1	0.16	0.04	0.1	0.08	0.05	0.07	0.05	0.17	0.05	0.07
REE	22.93	10.39	28.3	46.51	47.79	19.31	41.3	31.07	22.76	33.27	22.64	80.82	6.04	8.71
LREE/HREE	5.7	4.55	6.88	9.54	9.86	13.51	12.58	11.94	14.48	15.22	13.32	10.35	4.2	2.51
La/Ce	1.86	2.42	2.62	0.82	0.94	0.5	0.56	0.55	0.358	0.35	0.33	1.04	5.25	0.368
Ce/Ce*	0.28	0.24	0.2	0.53	0.64	1.04	0.94	0.94	1.41	1.34	1.33	0.47	0.11	0.94
Eu/Eu*	0.67	0.7	0.73	0.69	0.71	0.71	0.7	0.62	0.68	0.77	0.69	0.71	0.54	0.53
La _N /Nd _N	2.49	3.13	2.54	1.71	3.72	2.77	2.66	2.69	2.62	2.24	1.93	2.18	3.12	0.75
Dy _N /Yb _N	1.24	1.06	1.49	1.7	0.96	1.21	1.25	1.23	1.078	1.22	1.26	1.75	0.89	1.15
Ce _{anom}	-0.58	-0.68	-0.7	-0.269	-0.268	-0.016	-0.064	-0.061	0.12	0.11	0.12	-0.348	-1.024	-0.027
Ce _{SN} /Ce _{SN} *	0.28	0.23	0.2	0.52	0.62	1.02	0.92	0.92	1.38	1.32	1.31	0.11	0.87	0.47
Y _{SN} /Ho _{SN}	1.31	1.46	1.39	1.15	1.19	1.18	1.27	1.21	1.14	1.06	1.37	1.85	1.06	1.31
La _{SN} /Ce _{SN}	3.92	5.11	5.53	1.74	1.98	1.07	1.18	1.18	0.76	0.75	0.71	11.05	0.78	2.2
$Ce_{anom} = \text{Log} [3 * Ce_N / (2 * La_N + Nd_N)] *$														
$Ce^* = Ce_N / [2/3 La_N + 1/3 Pr_N] *$														
$Eu^* = Eu_N / [2/3 Sm_N + 1/3 Gd_N] *$														

203

204 found in the massive types of manganese deposits. This difference in behavior can be attributed
205 to the distinct geochemical properties of HFSE, leading to their unique distribution patterns in
206 the different types of manganese deposits.

207 The total rare earth elements content is very low (10.3 to 80 ppm), with a maximum of 80 ppm
208 observed in the vein type and the lowest concentration of 10.39 ppm in the massive types of
209 manganese deposits (Table 2). The chondrite normalized REE patterns generally exhibit flat
210 profiles, with negative anomalies for both Ce (-0.016 _ -1.024) and Eu (0.54 _ 0.71) observed
211 in most of the samples (Fig 3A). Moreover, when the REE patterns are normalized to the
212 composition of Post-Archean Australian Shale (PAAS), the samples show similar patterns with
213 Y positive anomalies, except that the intensity of the Eu negative anomaly is reduced (Fig 3B).

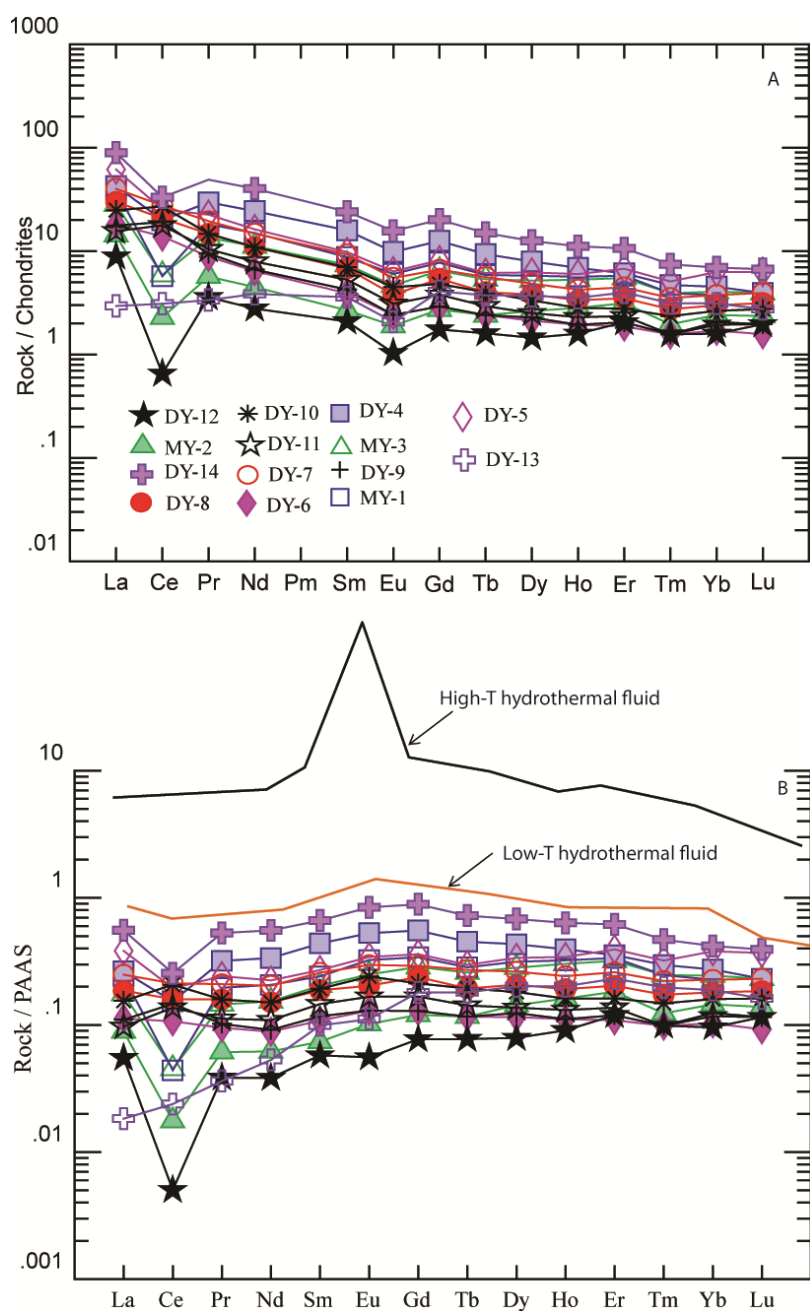
214 5. DISCUSSION

215 5.1. Elemental associations and their geochemical clue

216 5.1.1. Geostatistics: Principal component analysis (PCA)

217 There are different types of PCA methods, which include R-mode PCA and Q-mode PCA (Neff
218 1994). R-mode PCA primarily focuses on variables (elements in this study) and is suitable for
219 identifying associations between variables and a set of observations. On the other hand, Q-
220 mode PCA is mainly based on observations (samples, not shown in this study) and is used to
221 characterize multivariate observations and understand patterns among them. Principal
222 Component Analysis enables the identification of correlated element clusters (Neff, 1994). The
223 principal component and correlation matrices have been performed using the GEOstats Excel
224 sheet (Gündüz and Asan, 2022). The initial four principal components (PCs) encompass a
225 significant portion of the variances, reaching up to 93%. Notably, PC1, PC2, and PC3
226 encompass 83.6% of the total variability in the entire geochemical dataset. The principal
227 component PC1 (Fig 4) explains 67.63% of the total eigenvalues and primarily demonstrates

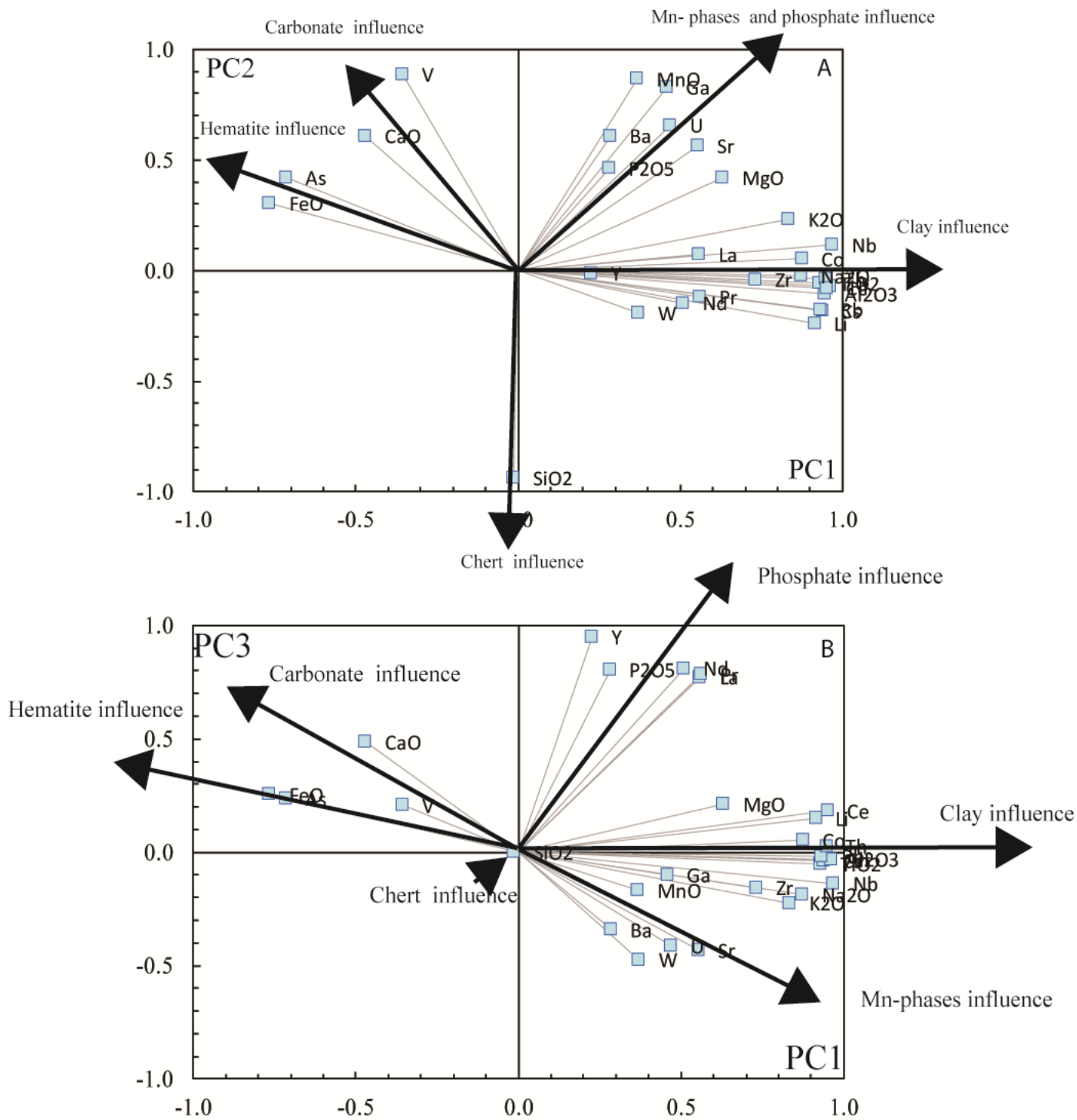
228 an anticorrelation between Fe and Mn. As a result, this axis closely aligns with the Fe-Mn side
229 of the Bonatti et al. 1972 triangle.



230

231 Fig 3. (A) REE patterns in manganese deposit samples from the Sulaimani metallogenic province, normalized to
232 chondrite values as per Sun and McDonough data from 1989. (B) REE patterns in manganese deposit samples
233 from the Sulaimani metallogenic province, normalized to Australian shale values as per McLennan's 1989. The
234 REE pattern of hydrothermal fluid from both high and low-temperature sources, as reported by Bau and Dulski
235 (1999).

236



237

238 Fig 4. A biplot graph displaying (A) Principal Component 1 (PC1) versus Principal Component 2 (PC2) for the
 239 Manganese dataset from the Sulaimani metallogenic provinces, (B) Principal Component 1 (PC1) versus Principal
 240 Component 3 (PC3) for the Manganese dataset from the Sulaimani metallogenic provinces. An arrow is used to
 241 indicate enrichment along this direction, in addition to the expected phase control.

242

243

244 After plotting the first three principal components (PCs) on the two biplots (Figs 4 A& B),
245 distinct patterns emerge. SiO₂ stands apart from other elements (Figs 4 A& B), exhibiting
246 anomaly conditions, **which reflect chert influence (Latif et al. 2022)**. Additionally, the biplots
247 of PC1 and PC2 versus PC3 reveal a strong correlation between REEs and major oxides like
248 Al₂O₃, Na₂O, and K₂O, suggesting that REEs are predominantly associated and hosted with
249 clay minerals and phosphates within the studied manganese deposit rather than the manganese
250 phases. Furthermore, a high correlation is observed between Fe and As, as well as between
251 CaO and V, which likely indicates their association with hematite and carbonate, respectively,
252 both of which are abundant in some rock samples. Moreover, MnO displays notable
253 correlations with Ga, Ba, P₂O₅, U, and Sr, suggesting that these elements are hosted in
254 manganese and phosphate phases within the deposit. The positive correlation with K₂O may
255 imply the potential presence of MgO within the montmorillonite crystal structure.

256 **5.1.2. Geostatic: Correlations coefficient**

257 A lack of notable positive correlation between SiO₂ and other primary elements may indicating
258 that SiO₂ predominantly occurs as microcrystalline quartz. This quartz is observed in the form
259 of chert within the studied region. The elevated concentration of CaO can be ascribed to the
260 presence of authigenic calcium. This calcium is liberated during the serpentinization process
261 of pyroxene and subsequently deposited as calcium carbonate in the extensive manganese ore
262 characteristic of the surveyed area (. Moreover, a conspicuous positive relationship is apparent
263 with alkali elements, specifically Na₂O and K₂O, suggesting their probable simultaneous
264 occurrence within distinct mineral phases, **probably in clay mineral**. The limited presence of
265 alkali elements suggests a minor impact from detrital phases rich in Na and K, like plagioclase
266 and pyroxene. This observation could imply that the deposition setting was far from continental
267 edges and their material contribution. Additionally, this might indicate that the source rock for

268 manganese is deficient in alkali elements, resembling more ultramafic rock compositions. The
269 lack of a distinct correlation with other significant oxide components suggests that MnO likely
270 exists as an independent phase within the analyzed specimens. This observation is reinforced
271 by X-ray diffraction data from Latif et al. (2022), which indicates a straightforward
272 composition of manganese minerals primarily comprised of MnO. The evident positive
273 correlation between CaO and Fe₂O₃ suggests that iron may be incorporated into the crystal
274 structure of carbonate minerals **as a siderite component**. The absence of a clear relationship
275 with other major oxides suggests that MnO occurs as a separate phase in the studied samples.
276 This observation is further supported by XRD data (Latif et al. 2022), which indicates that
277 manganese mineral composition is simple, consisting mainly of MnO. Indeed, the observation
278 of a very strong positive correlation between MnO and Ga in the samples suggests a significant
279 relationship between these elements. This correlation could imply that gallium is
280 predominantly hosted within the manganese phases present in the samples. It indicates that
281 there might be a close association between gallium and manganese minerals, and the presence
282 of manganese phases may contribute to the accumulation or incorporation of gallium in the
283 studied samples. The notable strong correlation between TiO₂ and Al₂O₃ implies that TiO₂
284 might be incorporated into the crystal structure of clay minerals. The weak positive correlation
285 between CaO and P₂O₅ indicates that there is very little contribution of phosphate minerals
286 associated with the Mn-bearing ore. The elevated content of BaO points toward the existence
287 of the mineral **barite**
288 within the massive deposits. This presence suggests a significant involvement of oceanic water
289 in the process of forming these deposits. The significant presence of Ni (with values exceeding
290 100 ppm) may suggest contributions from mafic-ultramafic rocks in the source rocks of
291 manganese deposits, especially in the massive type. The positive correlation among Zn, V, and
292 Ni indicates cogenetic geochemical behaviors among these elements. This correlation suggests

293 that they have a shared origin and may have been deposited together during the formation of
294 the manganese deposits in the studied area. LILEs are considered low ionic potential elements,
295 which means they tend to readily form inner sphere aqua complexes in aqueous solutions.
296 These elements are relatively large enough to be surrounded and coordinated by water
297 molecules, making them more soluble in aqueous solutions (Lee 2018). As a result, LILEs are
298 likely to be transported away from the mid-oceanic ridge (MOR) axis and reside farther from
299 it. The low contents of LILEs in the manganese deposits may be attributed to the original nature
300 of the manganese-producing reservoir, which is believed to be associated with the ultramafic
301 unit of ophiolite. This suggests that the source rocks for manganese in this area were rich in
302 ferromagnesian minerals, which influenced the abundance of LILEs in the deposits. However,
303 a majority of the samples exhibit distinct negative Ce anomalies, indicating the influence of
304 oceanic water. On the other hand, samples displaying slight positive Ce anomalies might be
305 linked to subsequent diagenetic alterations impacting these particular samples. This suggests
306 the possibility of certain diagenetic activities occurring after the initial deposition of these
307 samples. The consistent and uniform REE and PAAS pattern observed among various types of
308 manganese ore in the study area strongly suggests a cogenetic origin of the deposits. When the
309 REE patterns remain similar across different types of manganese deposits, it indicates that these
310 deposits likely share a common source of origin.

311

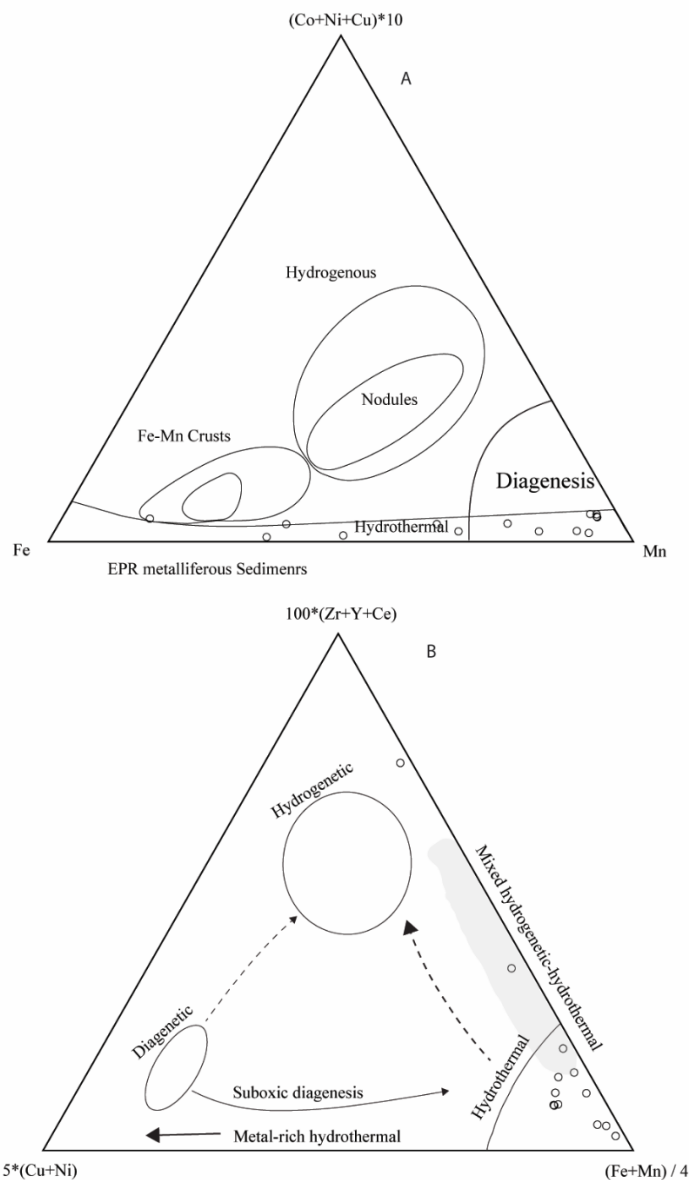
312 **5.2. Paleo redox**

313 In the study area, the Mn/Fe ratio in the Mn deposit ranges from 0.01 to 25.69. This range
314 indicates significant variability in the relative concentrations of manganese (Mn) and iron (Fe)
315 in the deposit. A Jasperite rock with Mn/Fe ratio of 0.01 suggests that the deposit is rich in iron
316 compared to manganese. This may indicate reducing conditions in the environment during the
317 formation of the jasperite, as iron tends to be more stable in its reduced form under such

318 conditions (Lepp, 1963). A Mn/Fe ratio of 25.69 in vein types indicates that the deposit is
319 abundant in manganese compared to iron. This may suggest oxidizing conditions in the
320 environment during the deposit formation, as manganese is more stable in its oxidized form
321 under such conditions (Lepp, 1963). The wide range of Mn/Fe ratios (from 0.01 to 25.69)
322 suggests that the redox conditions in the study area might have varied significantly during the
323 formation of the manganese deposit in Sulaimani metallogenic deposit. This variability could
324 be due to various factors, such as changes in the availability of oxygen, distance from the
325 manganese discharge sources. The immobile trace elements Co/Ni ratio of 0.34 in the studied
326 manganese samples indicates a reduced environment, further supporting the inference that the
327 manganese deposit is associated with a hydrothermal setting. Reduced environments are
328 commonly observed in hydrothermal systems where hot, mineral-rich fluids interact with
329 surrounding rocks, dissolving, and transporting metals like cobalt and nickel (Pirajno 2009,
330 Barnes 1997). The samples with Th/U ratio of less than 1 typically suggest a reducing or anoxic
331 environment (Krishnaswami and Lal. 1978). While samples with Th/U ratio of more than 1
332 often suggest an oxidizing or oxic environment (Krishnaswami and Lal. 1978). This variability
333 in Th/U ratio may indicate that the depositional environment likely underwent transitions
334 between oxic and anoxic conditions during the formation of the manganese deposit in the study
335 area. The range of Ce_{anom} values in the studied samples from -0.7 to 0.12 confirms the oxic to
336 anoxic nature of the Neotethys oceanic basin during the deposition of manganese. The presence
337 of both negative and positive Ce anomalies within this range suggests fluctuations in the redox
338 conditions in the ocean water during sedimentation (German and Elderfield 1990). This
339 variation can be associated with changes in oxygen levels, cyclic nature of the manganese
340 bearing hydrothermal fluid and organic matter deposition factors influencing the redox state of
341 the environment.

342 5.3. Genesis of the manganese deposit in the study area

343 Based on the trace elements geochemical data and the positioning of the ore samples within or
 344 close to the hydrothermal field in the ternary diagrams (Fe-Mn-(Ni + Cu + Co) *10 and 5(Cu
 345 + Ni)-100*(Zr + Y + Ce)-((Fe + Mn)/4), it is reasonable to classify the manganese ore in the
 346 study area as a hydrothermal type manganese ore deposit (Figs 5A and B).

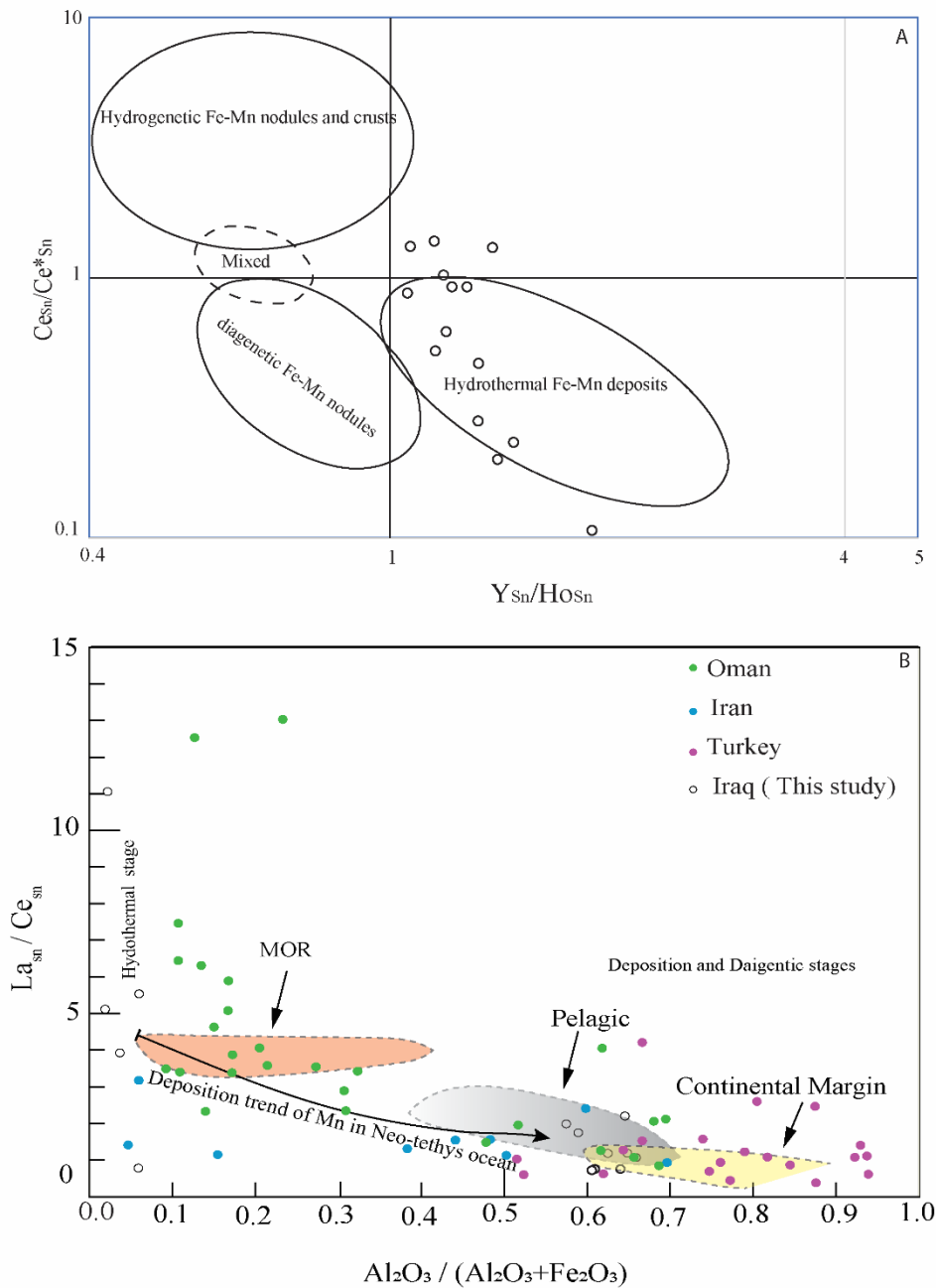


347
 348 Fig 5. A ternary manganese discrimination based on (A) (Cu + Ni + Co) * 10 - Fe - Mn (after Bonatti et al.
 349 (1972) and later refined by Crerar et al. (1982), (B) (Fe+Mn)/4 - 5*(Cu+Ni) - 100*(Zr+Y+Ce) (after Josso et al.
 350 2017). It is used to categorize and differentiate manganese occurrences in Sulaimani metallogenic district.

351
 352

353 The Co/Zn ratios in the analyzed samples vary from 0.01 to 2.22, with an average of 0.94.
354 Hydrothermal Mn deposits typically have Co/Zn ratios around 0.15, whereas hydrogenous Mn
355 deposits have Co/Zn ratios higher than 2.5 (Usui et al. 2017). Comparing the average Co/Zn
356 ratio of 0.94 in the studied samples to the values seen in hydrothermal Mn deposits, it falls
357 within the range typical for hydrothermal deposits. This suggests that the Mn deposit in the
358 study area is **primarily** linked with hydrothermal activity, **despite late minor diagenetic**
359 **overprint**. The presence of ore samples within or near the hydrothermal field on these ternary
360 diagrams suggests that the manganese mineralization in the study area is likely associated with
361 hydrothermal activity. Hydrothermal deposits are formed through the interaction of hot,
362 mineral-rich fluids with the surrounding rocks serpentinite parent rocks in the study area along
363 the paleo MOR. These fluids are typically derived from oceanic sources circulating through
364 fractures and faults along a ridge axis. In a hydrothermal setting, as the hot fluids come into
365 contact with the host rocks, they dissolve and carry away various elements, including **Mn, Ni,**
366 **Cu, Co, Zn,** and other trace elements. When these fluids cool down by **seawater**, they precipitate
367 out minerals, leading to the formation of manganese ore deposits (Morgan, 2005). The REE
368 contents in the manganese deposit in the study area range from 6.04 to 80.82 ppm, with an
369 average of 30.13 ppm across all samples. The data suggest that the total REE of the studied
370 deposit is relatively low. This means that the concentration of rare earth elements in the
371 manganese deposit is not as high as those found in some other types of deposits, particularly
372 hydrogenous deposits. The REE pattern of the samples from the Mn deposit in the study area
373 corresponds to that of hydrothermal deposits. Hydrothermal Mn-oxides typically exhibit
374 modest REE compositions, with total REE content around 100 ppm. This pattern is in contrast
375 to hydrogenous deposits, where the total REE content is significantly higher, often exceeding
376 1000 ppm (**Bau et al., 2014**). Moreover, the biplot of Ce_{sn}/Ce^*_{sn} vs. Y_{sn}/Ho_{sn} show that all
377 studied samples plot in the field of hydrothermal-type Mn deposits (**Bau et al., 2014**) (Fig 6A).

378 Overall, the geochemical data and analyses suggest that the manganese deposit in the study
 379 area is characterized by relatively low total REE content and exhibits geochemical signatures
 380 consistent with hydrothermal-type Manganese deposits.



381

382 Fig 6. (A) REE based manganese discrimination diagram Ce_{SN}/Ce_{SN^*} vs. Y_{SN}/HO_{SN} , as presented by Bau et al.
 383 (2014), provide supporting evidence for the hydrothermal origin of manganese deposits found in the Sulaimani
 384 metallogenic deposit. B) La_n/Ce_n vs. $Al_2O_3 / (Al_2O_3 + Fe_2O_3)$, tectonic discrimination diagram for manganese ores
 385 in the Zagros region. Normalizing values are from (Evensen et al. 1978). the data source for Oman, Iran, and
 386 Turkey area explained elsewhere in the text.

387 **5.4. Nature of Hydrothermal fluid**

388 When hydrothermal fluids are generated through high-temperature processes, they exhibit a
389 pronounced positive europium anomaly (Michard1989; Bau and Dulski1999). The positive Eu
390 anomaly indicates that europium is preferentially mobilized and enriched in the hydrothermal
391 fluids under these conditions. This phenomenon has been observed and studied in various
392 geological settings encompasses high-temperature hydrothermal fluid (Bau and Dulski 1999).
393 In contrast, hydrothermal fluids produced by low-temperature hydrothermal alteration do not
394 show a significant Eu anomaly or may not have one at all (Bau and Dulski 1999). The absence
395 or weak expression of the Eu anomaly in these fluids is characteristic of the geochemical
396 processes taking place at lower temperatures in addition to lack of plagioclase in the source.
397 The absence of sharp positive europium anomalies in the geochemical signature of the
398 manganese deposits in the study area confirms the involvement of low-temperature
399 hydrothermal fluids in their formation (Fig 6B).

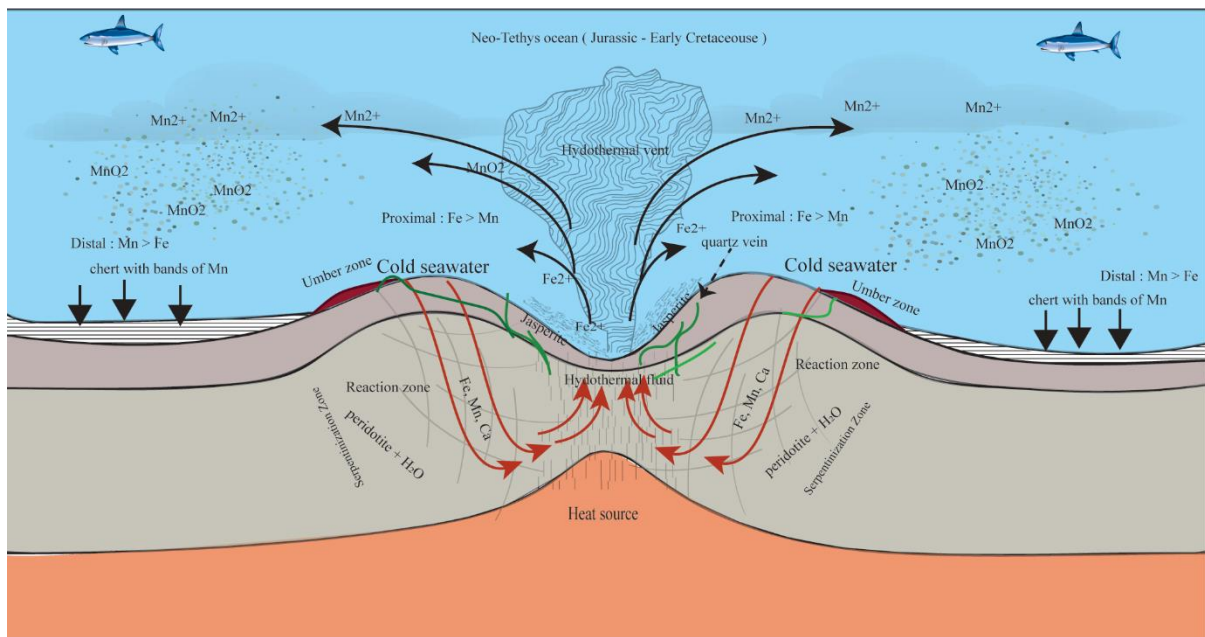
400

401 **5.5. Proposed Model for the Mn²⁺ source in the area and tectonic setting**

402 Chen et al. (2018 and reference there in) propose a variety of potential sources for manganese
403 (Mn) deposits. These sources include seawater, hydrothermal-exhalative processes, exhalative-
404 terrigenous inputs, lower crust/mantle contributions, volcanic ash, and oceanic magmato-
405 sedimentary sources. **Since serpentized harzburgite is the predominant altered rock in the**
406 **study area, this study ultimately suggests that the Mn, Fe and other metals in the area are**
407 **primarily derived from ultramafic rocks through a serpentization process. Moreover, the low**
408 **total rare earth elements and alkali elements, combined with elevated Ni contents in the**
409 **manganese deposit in the area, support the idea that ultramafic rock could be the best candidate**
410 **for the parent material.**

411 Low total REE in addition and alkile elements in addition to elevated Ni contents in manganese
 412 deposit in the area in support for ultramafic rock to be a best candidate. During serpentinization,
 413 water interacts with ultramafic rocks (Fig 7), which are rich in magnesium and iron. This
 414 interaction leads to the formation of serpentine minerals and the release of various elements,
 415 including Mn, Fe and other metals. The proposed model describes.

416



417

418 Fig 7. A proposed model after Latif et al. (2022), explaining the genesis of manganese deposits linked to **Neotethys**
 419 radiolarite involves the infiltration of cold deep seawater through fractures in a weakened zone along the Mid-
 420 Ocean Ridge (MOR) reaction zone within the crust-upper mantle segment of the **Neotethys** oceanic crust.

421

422 the occurrence of an ultramafic harzburgite body in a mid-oceanic ridge setting within the
 423 Penjween ophiolite. The upper mantle unit of the ophiolite undergoes varying degrees of
 424 serpentinization due to the infiltration of deep seawater through fractures in the oceanic crust
 425 before obduction (Mohammad 2011). In the reaction zone, the infiltrated seawater reacts with
 426 the ultramafic rocks, leading to the formation of syn serpentinization fluid enriched in Fe, Mn,
 427 Ca, and Mg (Mohammad 2011) **via leaching**. This heated fluid becomes buoyant and is rapidly
 428 discharged to the ocean floor through plumes and vents or by infiltrating through additional

429 fractures. Mixing with seawater results in the formation of diffuse hydrothermal fluid enriched
430 in Mn and Fe. The proposed model aligns with previous research findings. Mineral chemistry
431 data obtained from meta harzburgite of the Penjween ophiolite reveal the manganese content
432 in the parent minerals. The original olivine contains up to 0.4 wt. % MnO, while the chromian
433 spinel contains up to 1.2 wt. % MnO (Mohammad 2011). During the hydrothermal alteration
434 process, the parent minerals undergo transformation into new minerals. The chromium
435 magnetite and serpentine formed from the alteration of olivine and chromian spinel,
436 respectively, exhibit decreasing MnO content. The chromium magnetite contains about 0.1 wt.
437 % MnO, and the serpentine contains about 0.25 wt. % MnO (Mohammad 2011). Combining
438 rare earth element (REE) data with the $Al_2O_3 / (Al_2O_3 + Fe_2O_3)$ ratios provides a useful method
439 to determine the depositional tectonic environment of manganese ores, as demonstrated by Xie
440 et al. (2013) using a L_{sn}/C_{sn} vs. $Al_2O_3 / (Al_2O_3 + Fe_2O_3)$ tectonic discrimination plot (Fig 5B)
441 (Murray's 1994).

442 In the context of the Zagros manganese deposits, the samples fall within a specific range on
443 the discrimination plot, spanning between fields associated with spreading ridge proximal
444 manganese deposits and a distal pelagic field to a continental margin. This suggests that most
445 of the manganese deposits along the Zagros orogeny likely originated from a proximal-distal
446 hydrothermal source with the **Neotethys** oceanic basin. Furthermore, this finding supports the
447 idea that all manganese deposits associated with radiolarite chert facies, from Oman to Turkey,
448 are linked to regional mid-oceanic ridge hydrothermal activity within **Neotethys** rather than
449 local volcanic activity. The geochemical data from Oman, Turkey, and Iran are (Robertson and
450 Fleet (1986) for Oman, Oksüz (2011) for Turkey, and Zarasvandi (2016) for Iran.

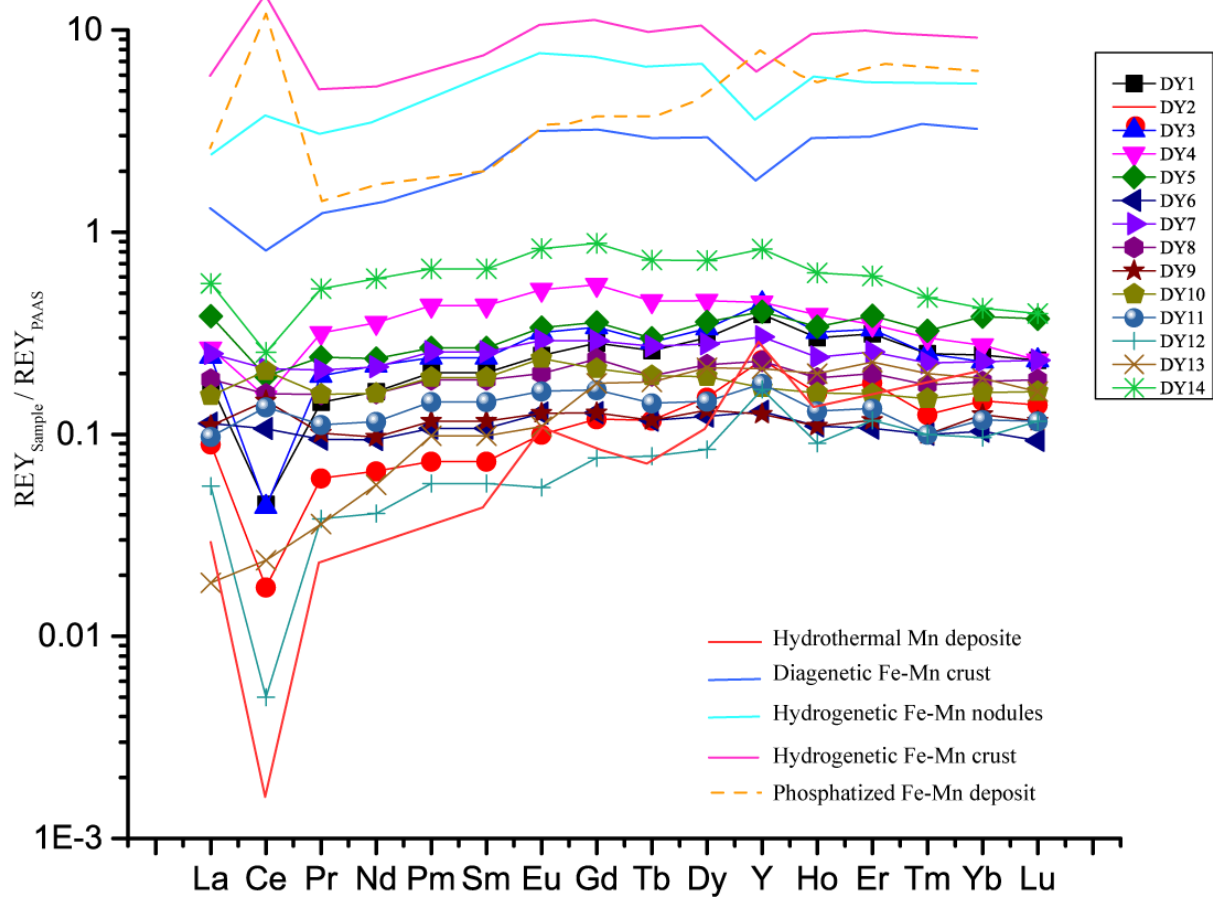
451

452

453 **5.6. Manganese nodules problem in the area**

454 Manganese nodules are deposits that form in situ (authigenic) and through diagenesis
455 (diagenetic) (Hein 2016; Usui et al. 1993; Cronan1997). They mainly consist of manganese
456 oxides and contain significant amounts of Fe, Co, REE, Ni, and Cu. These nodules are
457 distributed throughout all the oceans worldwide, but they are typically found in regions
458 characterized by slow sediment accumulation and a wide ocean floor. There are two primary
459 types of manganese nodules: hydrogenous, which originate from seawater, and diagenetic,
460 which are the result of redox reactions occurring during sediment diagenesis. The formation of
461 manganese nodules is relatively straightforward, involving the precipitation of metal
462 compounds dissolved in seawater around a nucleus on the ocean floor. This growth can occur
463 in two ways: hydrogenous growth happens near the sediment-water interface as metal
464 compounds sink and precipitate, while diagenetic growth occurs within the sediments
465 themselves through the remobilization and reprecipitation of manganese along faults and low-
466 strain zones with high porosity and permeability in the host rock.

467 These two types of nodules, hydrogenous and diagenetic, exhibit distinct differences in their
468 geochemical composition and internal structure. Hydrogenous nodules show well-developed
469 internal layering around nuclei and contain higher levels of Cr, Cu, Ni, and total rare earth
470 elements with a positive cerium anomaly. On the other hand, diagenetic nodules lack complex
471 internal structures, have lower levels of **Cr, Cu, Ni**, and total REE, and generally display weak
472 **negative** cerium anomalies (Fig 8). By integrating petrographic analysis with the rare earth
473 element pattern, it is possible to propose that the manganese macro-nodule in the study area is
474 of diagenetic origin.



475

476 Fig 8. REY_{SN} patterns of various manganese deposit types in the Sulaimani metallogenic deposits, juxtaposed
 477 with patterns from marine hydrothermal Fe and Mn deposits, diagenetic Fe-Mn nodules, hydrogenetic Fe-Mn
 478 nodules, hydrogenetic Fe-Mn crusts, phosphatized hydrogenetic Fe-Mn crusts. The data for this comparison is
 479 sourced from Bau et al. (1996), with values normalized according to McLennan (1989). These patterns are used
 480 to analyze and differentiate the geochemical characteristics of manganese deposits in the Sulaimani region in
 481 comparison to other types of deposits.

482 Throughout the diagenetic alterations of the manganese-rich beds containing chert, ore
 483 minerals were remobilized during deformation events, leading to the formation of centimeter-
 484 scale nodules of pyrolusite. Additionally, the presence of rhythmic alternations between quartz-
 485 rich chert beds and clay-rich interbeds, around the manganese rich layer indicates a significant
 486 differential diagenetic modification of the radiolarite chert in the studied region (Abrajevitch,
 487 2020).

488

489

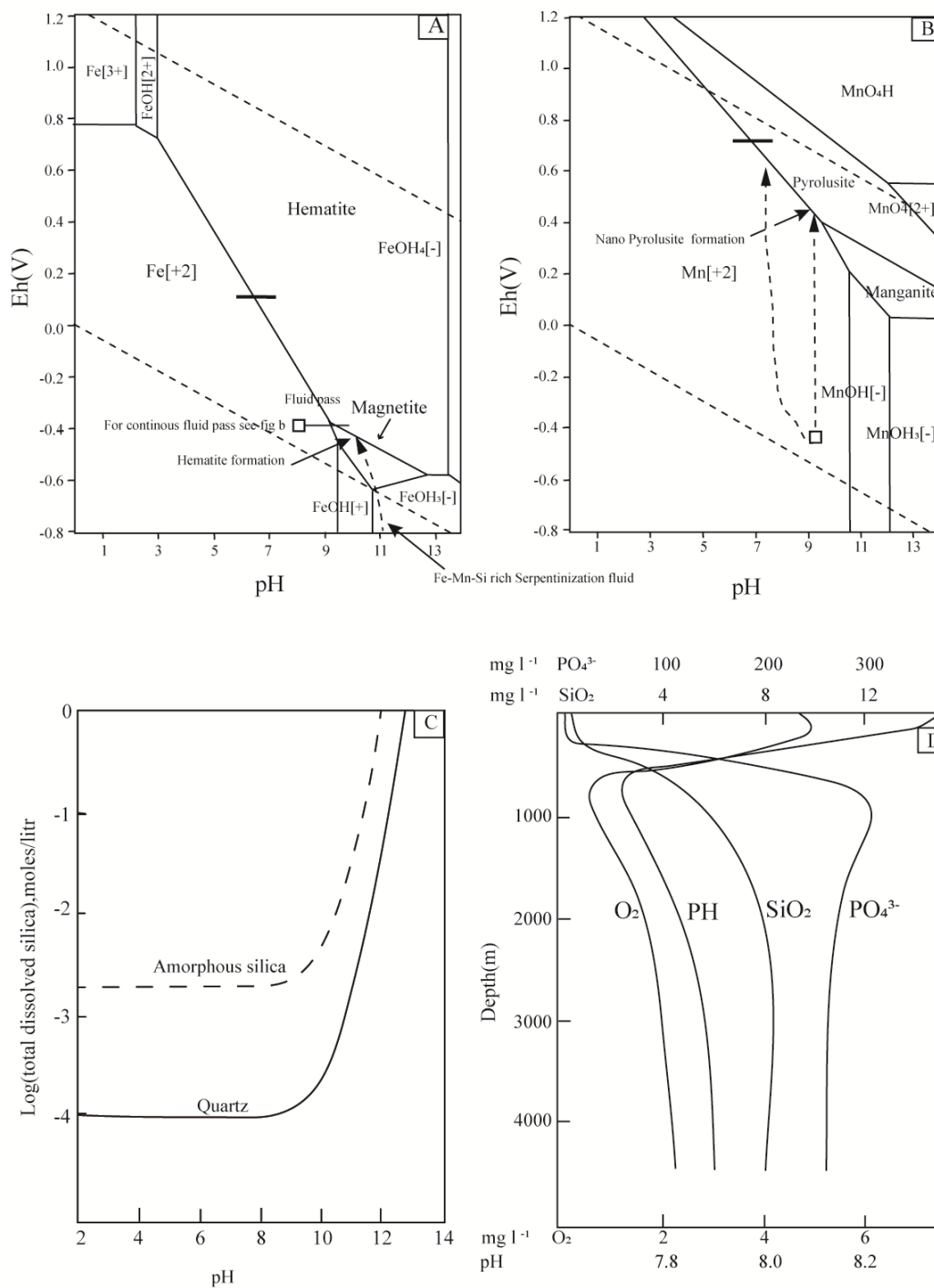
490 **5.7. Eh-PH diagram and mechanism of Fe-Mn-Si depositions in Neotethys.**

491 To identify the paleo-oceanography and depositional settings of Fe-Mn-Si elements that are
492 released via hydrothermal solutions along the Neotethys ridge axis, an Eh-pH diagram can
493 serve as a useful tool (Fig.9 A-B) (Glasby and Schulz 1999). This diagram helps trace the
494 formation and stability of the expected Fe-Mn-Si phases in the Neotethys oceanic basin as
495 follow:

496 Serpentinization is a widespread geochemical process where peridotite undergoes aqueous
497 alteration to transform into serpentine minerals along the MOR (Kelley et al. 2001; Früh-Green
498 et al. 2004). The fluid produced during serpentinization is characterized by relatively high pH
499 levels (ranging from 10.9 to 12) and low concentrations of Si, Mg, Fe, and Mn, while having
500 high concentrations of Na, K, Ca, and Cl⁻ (Charlou et al. 2002; Kelley et al. 2001)

501 As the fluid is released along the vents in the mid-ocean ridge axis, the Fe components of the
502 fluid react with the low oxygen content of the ocean bottom environments, under low Eh
503 (oxidation-reduction potential) conditions around -0.2 V. This leads to the formation of
504 hematite (Fig 9A), as hematite tends to favor less oxidized environments.

505 At the same time, manganese occurs as Mn ions in the hydrothermal fluid. When the high pH
506 hydrothermal fluid mixes with the moderate pH conditions of the ocean (pH 7.9, Fig 9D), it
507 undergoes a shift to a lower pH solution (pH 7-8). This shift is a result of homogenization
508 processes occurring near the ocean bottom. As a consequence, silica (SiO₂) is deposited in the
509 form of jasper or microcrystalline quartz (Fig 9C). This deposition can lead to the formation of
510 jasperite near the discharge area. In the studied area, the co-occurrence of hematite and quartz
511 in the form of jasperite can be observed, either as patches in metabasalt or as layers above
512 basaltic rocks. On the Eh-pH diagram (Fig 9B), the formation of Mn-minerals (manganese
513 deposits) can follow two possible scenarios and paths:



514

515 Fig 9. Manganese and iron precipitation mechanism to form various phases in the study area (A) Eh-pH stability
 516 diagram for Fe (B) Eh-pH stability diagram for Mn species (Diagrams after Brookins 1988, Force and Cannon
 517 1988), (C) Solubility of SiO₂ vs. pH calculated from thermodynamic value given by Weast and Astle 1986(D)
 518 SiO₂, PO₄, O₂ and pH profile of oceanic water column (Schlesinger and Bernhardt 2013). The precipitation trend
 519 of hematite and pyrolusite shown on Fig 8A and B.

520

521 Scenario 1: Under conditions of low Eh (low oxygen) and high pH, as indicated on the Eh-pH
522 diagram (Fig 9B), the first manganese (Mn) mineral to form will be manganite among the
523 manganese phases. It is likely and expected to be found in association with hematite or close
524 to the location where hematite has been deposited. Over time, through the process of diagenesis
525 and oxidation, manganite will undergo solid-state oxidation and be converted into pyrolusite
526 (Dupont and Donne 2014).

527 Scenario 2: In environments with high Eh (moderate to highly oxidized conditions) and low
528 pH, to form manganese dioxide in the form of pyrolusite, the aqueous environment requires
529 oxidation (e.g., $Eh > 0.5$ V at pH ~ 8). The possible oxidants in oceanic water include molecular
530 oxygen, ozone, nitrates, and perchlorate acids. These oxidants can be produced through
531 photochemical processes (Noda et al. 2019). However, these oxidants are generally low in
532 concentration near the ocean bottom. As a result, the likelihood of pyrolusite deposition near
533 the ocean bottom, particularly close to the fluid discharge site, is low. Due to the slow settling
534 time of Mn in solution (Lupton et al. 1980), it tends to rise from the discharging area at the
535 bottom of the oceanic water. As it ascends, it becomes enriched in the rising plume active area
536 in the ocean, above the ocean bottom. Eventually, it reaches a certain oxidized zone in the water
537 column, where it reacts with oxygen to form MnO nuclei.

538 The nucleation process of the MnO nuclei may lead to the formation of pyrolusite nanoparticles
539 (e.g. Graca et al 2018). This occurs far from the discharge area, in the oxidizing ocean zone.
540 These pyrolusite nanoparticles, due to their small size, remain suspended in the water column
541 for some time. However, eventually, they precipitate due to gravitational forces and settle as
542 nanoparticles on the ocean bottom, away from the ridge axis (e.g. Yücel et al. 2011, González-
543 Santana et al. 2020). This settling and precipitation of pyrolusite nanoparticles on the ocean
544 bottom led to the development of bands or layers rich in pyrolusite. These bands form at a
545 distance from the ridge axis, where the nanoparticles have settled and accumulated over time.

546 The absence of any preexisting manganite as relict or patches, along with the difficulty of
547 preserving the high pH of serpentinization fluid due to mixing with low pH oceanic water and
548 silica deposition (Figs 9C and D), leads to the conclusion that the first scenario is less likely to
549 be the dominant depositional process of manganese formation in Neotethys ocean basin.

550 Instead, this study favors the second scenario as the dominant process of manganese formation
551 in the area, especially near Kani Safi village. The presence of pyrolusite in nano-particle form,
552 as reflected in the banding nature of manganese deposits in the study area, supports the idea
553 that the manganese was formed through the second scenario. The formation of pyrolusite
554 nanoparticles far from the hydrothermal fluid discharge area, within the oxidizing ocean zone,
555 and their subsequent precipitation on the ocean bottom, explains the observed distribution and
556 characteristics of the manganese deposits in the **Sulaimani** metallogenic deposit as a part of
557 Neotethys ocean basin.

558 The cyclic nature of hydrothermal vents along the mid-ocean ridge (MOR) results in a
559 continuous variation of Eh-pH conditions in the depositional environment (**Haymon et al.** 1993;
560 **German et al.** 1996). This dynamic environment may contribute to the formation of successive
561 layers containing pyrolusite-rich and pyrolusite-free sections. Such cyclic patterns in the form
562 **of layered (laminae) type manganese** deposit have been observed not only in the study area but
563 also in other parts of the manganese deposit with the Neotethys oceanic basin (**Maghfouri et al.**
564 **2019**). As hydrothermal fluids are periodically released from the vents, they interact with the
565 surrounding oceanic water, leading to fluctuations in the redox potential (Eh) and pH levels.
566 These changes influence the mineral formation processes, including the precipitation and
567 deposition of manganese minerals like pyrolusite. Consequently, the manganese-rich layers are
568 formed during periods of favorable conditions for pyrolusite nucleation and growth, while
569 pyrolusite-free layers may occur when the conditions are not suitable for its formation.
570 Moreover, these cyclic nature hydrothermal vents highlight the significance of the

571 hydrothermal vent activity in shaping the manganese deposition and mineralogical
572 characteristics in the area.

573 **6. Conclusions**

574 The presence of various modes of occurrence and the syngenetic and diagenetic origins suggest
575 a complex geological history and a combination of processes contributing to the formation of
576 manganese deposits in the Sulaimani metallogenic province. The multi-trace and REE
577 discriminations signature, coupled with a REE chondrite normalized pattern observed in the
578 majority of samples, indicates that submarine hydrothermal processes have likely played a
579 significant role in the deposition of the Fe-Mn belt in the study area. The compilation of
580 geochemical data from diverse manganese deposits linked to the **Neotethys** radiolarite chert
581 facies, spanning from Oman to Turkey, indicates a predominant association with hydrothermal
582 activity along mid-oceanic ridges. This suggests that these deposits are likely connected to such
583 ridge-related processes rather than being influenced by alternative tectonic settings or genetic
584 processes. The deposition of manganese, iron, and silica within the **Neotethys** oceanic basin is
585 primarily controlled by the Eh-pH conditions. These conditions play a significant role in
586 influencing the precipitation and accumulation of these elements. The cyclic activity of
587 hydrothermal vents along the mid-oceanic ridges further contributes to the continuous variation
588 in Eh-pH conditions in the depositional environment. The close association of serpentinite and
589 radiolarite bearing manganese deposits may verify a temporary and spatial relationship
590 between these two types of rocks. The serpentinization of ultramafic units and subsequent
591 hydrothermal alteration played a crucial role in providing a significant source of manganese
592 and silica, contributing to the formation of manganese deposits in the studied area and the entire
593 radiolarite facies within the **Neotethys** realm.

594

595 **Acknowledgment**

596 The authors are very grateful to Dr. N. Daneshvar from Kurdistan University, Iran are highly
597 appreciated for their fruitful discussions and help. Thank you to the four anonymous
598 reviewers for their invaluable feedback and insightful comments, which have improved the
599 quality of this work. Special appreciation goes to Editor-in-Chief Dr. Rahim Dabri for his
600 invaluable guidance in overseeing the paper and providing insightful advice on the early
601 versions.

602

603 **Conflicts of interest**

604 The authors declare that they have no conflicts of interest.

605

606 **Reference**

607 Al-Bassam, KS (1984) Final report on the regional geological survey of Iraq. vol. 5 *Economic geology*
608 *of Iraq*.

609 Al-Bassam, KS (2013) Mineral Resources of Kurdistan Region, Iraq. *Iraqi Bulletin of*
610 *Geology and Mining* 9:103–127.

611 Abrajvitch A (2020) Diagenetic formation of bedded chert: Implications from a rock magnetic study
612 of siliceous precursor sediments. *Earth and Planetary Science Letters* 533:116039.

613 Aydoğan, MS (2021) The Tafak manganese deposit (Dursunbey-Balıkesir, NW Turkey): implications
614 for the submarine hydrothermal origin of İzmir-Ankara-Erzincan Neotethyan Ocean. *Arabian*
615 *Journal of Geosciences* 14: 2321.

616 Barnes, HL (1997) *Geochemistry of hydrothermal ore deposits*. John Wiley & Sons, United States of
617 America.

618 Bau M, Koschinsky A, Dulski P, Hein JR (1996) Comparison of the partitioning behaviours of yttrium,
619 rare earth elements, and titanium between hydrogenetic marine ferromanganese crusts and
620 seawater. *Geochimica et Cosmochimica Acta* 60:1709–1725.

621 Bau M, Dulski P (1999) Comparing yttrium and rare earths in hydrothermal fluids from the Mid-
622 Atlantic Ridge: implications for Y and REE behavior during near-vent mixing and for the Y/Ho
623 ratio of Proterozoic seawater. *Chemical Geology* 155:77–90

624 Bau M, Schmidt K, Koschinsky A, Hein J, Kuhn T, Usui A (2014) Discriminating between different
625 genetic types of marine ferro-manganese crusts and nodules based on rare earth elements and
626 yttrium. *Chemical Geology* 381:1–9.

627 Baziany MM (2014) Depositional systems and sedimentary basin analysis of the qulqula radiolarian
628 formation of the zagros suture zone, sulaimani area, Iraqi kurdistan region. Unpublished Ph. D.
629 Thesis, university of sulaimani.

630 Bonatti E, Fisher D, Joensuu O, Rydell H, Beyth M (1972) Iron-Manganese-Barium Deposit from the
631 Northern Afar Rift (Ethiopia). *Economic Geology* 67:717–730

632 **Brookins DG (1988) Eh-pH Diagrams for Geochemistry. Springer Berlin Heidelberg, Berlin,**
633 **Heidelberg.**

634 Buday T, Jassim SZ (1984) Tectonic map of Iraq, scale 1: 1000 000. *Geological Survey and Mineral*
635 *Investigation*. Baghdad.

636 Chen F, Wang Q, Yang S, Zhang Q, Liu X, Chen J, Carranza EJM (2018) Space-time distribution of
637 manganese ore deposits along the southern margin of the South China Block, in the context of
638 Palaeo-Tethyan evolution. *International Geology Review* 60:72–86.

639 Charlou JL, Donval JP, Fouquet Y, Jean-Baptiste P, Holm N (2002) Geochemistry of high H₂ and CH₄
640 vent fluids issuing from ultramafic rocks at the Rainbow hydrothermal field (36°14'N, MAR).
641 *Chemical Geology* 191:345–359.

642 Crerar DA, Namson J, Chyi MS, Williams L, Feigenson MD (1982) Manganiferous cherts of the
643 Franciscan assemblage; I, General geology, ancient and modern analogues, and implications
644 for hydrothermal convection at oceanic spreading centers. *Economic Geology* 77:519–540.

645 Cronan DS (1977) Deep-sea nodules: distribution and geochemistry, in: Elsevier Oceanography Series.
646 Elsevier, pp. 11–44.

647 De Wever P, Bourdillon-de Grissac C, Bechenec F (1988) Permian age from radiolarites of the
648 Hawasina nappes, Oman Mountains. *Geology* 16:912–914.

649 Dupont MF, Donne SW (2014) Nucleation and Growth of Electrodeposited Manganese Dioxide for
650 Electrochemical Capacitors. *Electrochimica Acta* 120:219–225.

651 Evensen NM, Hamilton PJ, O’Nions RK (1978) Rare-earth abundances in chondritic meteorites.
652 *Geochimica et Cosmochimica Acta* 42:1199–1212.

653 Force ER, Cannon WF (1988) Depositional model for shallow-marine manganese deposits around
654 black shale basins. *Economic Geology* 83:93–117.

655 Force ER, Cannon WF (1988) Depositional model for shallow-marine manganese deposits
656 around black shale basins. *Economic Geology* 83:93–117.

657 Fouad SF (2012) Western Zagros fold–thrust belt, part I: The low folded zone. *Iraqi*
658 *Bulletin of Geology and Mining* 5: 39–62.

659 Früh-Green GL, Connolly JA, Plas A, Kelley DS, and Grobéty B (2004) Serpentinization of oceanic
660 peridotites: implications for geochemical cycles and biological activity. The subseafloor
661 biosphere at mid-ocean ridges 144:119-136.

662 German CR, Elderfield H (1990) Application of the Ce anomaly as a paleoredox indicator: the ground
663 rules. *Paleoceanography* 5:823–833.

664 German C, Klinkhammer G, Rudnicki M (1996) The Rainbow hydrothermal plume, 36°15’N, MAR.
665 *Geophysical Research Letters* 23(21):2979-82.

666 Glasby GP, Schulz HD (1999) Eh Ph diagrams for Mn, Fe, Co, Ni, Cu and as under seawater
667 conditions: application of two new types of eh ph diagrams to the study of specific problems
668 in marine geochemistry. *Aquatic Geochemistry* 5:227-48.

669 González-Santana D, Planquette H, Cheize M, Whitby H, Gourain A, Holmes T, Guyader V,
670 Cathalot C, Pelleter E, Fouquet Y, Sarthou G (2020) Processes driving iron and manganese
671 dispersal from the TAG hydrothermal plume (Mid-Atlantic Ridge): results from a
672 GEOTRACES process study. *Frontiers in Marine Science* 7: 568.

673 Graca B, Zgrundo A, Zakrzewska D, Rządziejewicz M, Karczewski J (2018) Origin and fate of
674 nanoparticles in marine water—Preliminary results. *Chemosphere* 206: 359-368.

675 GündüzM, Asan K (2022) GEOstats: an excel-based data analysis program applying basic principles
676 of statistics for geological studies. *Earth Science Informatics* 15: 705-712.

677 Haymon RM, Fornari DJ, Von Damm KL, Lilley MD, Perfit MR, Edmond JM, Shanks WC, Lutz
678 RA, Grebmeier JM, Carbotte S, Wright D, McLaughlin E, Smith M, Beedle N, Olson E
679 (1993) Volcanic eruption of the mid-ocean ridge along the East Pacific Rise crest at 9°45–
680 52'N: Direct submersible observations of seafloor phenomena associated with an eruption
681 event in April, 1991. *Earth and Planetary Science Letters* 119:85–101.

682 **Hein JR (2016) Manganese nodules. *Encyclopedia of marine geosciences*, 408-412.**

683 Hein JR, Schwab WC, Davis A (1988) Cobalt-and platinum-rich ferromanganese crusts and
684 associated substrate rocks from the Marshall Islands. *Marine Geology* 78:255–283.

685 Jassim SZ, Goff JC (2006) *Geology of Iraq*. DOLIN, distributed by Geological Society of London.

686 Josso P, Pelleter E, Pourret O, Fouquet Y, Etoubleau J, Cheron S, Bollinger C (2017) A new
687 discrimination scheme for oceanic ferromanganese deposits using high field strength and rare
688 earth elements. *Ore Geology Reviews SI: Marine mineral deposits: New resources for base,*
689 *precious, and critical metals* 87:3–15.

690 **Krauskopf KB (1957) Separation of manganese from iron in sedimentary processes. *Geochimica et*
691 *Cosmochimica Acta*, 12: 61-84.**

692 Kelley DS, Karson JA, Blackman DK, FruÈh-Green GL, Butterfield DA, Lilley MD, Olson EJ,
693 Schrenk MO, Roe KK, Lebon GT (2001) An off-axis hydrothermal vent field near the Mid-
694 Atlantic Ridge at 30 N. *Nature* 412:145–149.

695 Kickmaier W, Peters TJ (1990) Manganese occurrences in the Al Hammah Range—Wahrah
696 Formation, Oman Mountains. *Geological Society, London, Special Publications* 49:239–249.

697 Krishnaswami S, Lal D (1978) Radionuclide limnology, in: *Lakes: Chemistry, Geology, and*
698 *Physics*. Springer, pp. 153–177.

699 Latif D, Mohammad Y, Baziany M (2021) Mineralogy and Origin of the Manganese Deposit in the
700 Sulaimani Province, Kurdistan Region of Iraq: Insight to Serpentinization-Induced
701 Manganese Production Scenario. *Iraqi Geological Journal* 55:178–200.
702 <https://doi.org/10.46717/igj.55.1F.15Ms-2022-06-30>

703 **Lee CT (2018) Geochemical classification of elements. *Encyclopedia of Geochemistry. Encyclopedia*
704 *of Earth Sciences Series*. Springer**

705 Lepp H (1963) The relation of iron and manganese in sedimentary iron formations. *Economic*
706 *Geology* 58: 515-526.

707 Lupton JE, Klinkhammer, GP, Normark WR, Haymon R, MacDonald KC, Weiss RF, Craig H (1980)
708 Helium-3 and manganese at the 21°N East Pacific Rise hydrothermal site. *Earth and*
709 *Planetary Science Letters* 50:115–127. [https://doi.org/10.1016/0012-821X\(80\)90123-5](https://doi.org/10.1016/0012-821X(80)90123-5)

710 Maghfouri S, Rastad, E, Movahednia M, Lentz DR, Reza Hosseinzadeh M, Ye L, Mousivand F
711 (2019) Metallogeny and temporal–spatial distribution of manganese mineralizations in Iran:
712 Implications for future exploration. *Ore Geology Reviews* 115, 103026.

713 McLennan SM (1989) Rare earth elements in sedimentary rocks; influence of provenance and
714 sedimentary processes. *Reviews in Mineralogy and Geochemistry* 21:169–200.

715 Michard A (1989) Rare earth element systematics in hydrothermal fluids. *Geochimica et*
716 *Cosmochimica Acta* 53:745–750.

717 Mohammad YO, Maekawa H, Lawa FA (2007) Mineralogy and origin of Maekawa albitite from
718 Kurdistan region, northeastern Iraq. *Geosphere*, 3: 624-645.

719 Mohammad YO (2011) Serpentinites and their tectonic signature along the Northwest Zagros Thrust
720 Zone, Kurdistan Region, Iraq. *Arabian Journal of Geosciences* 4:69–83.

721 Mohammad YO, Cornell DH, Qaradaghi JH, Mohammad FO (2014). Geochemistry and Ar–Ar
722 muscovite ages of the Daraban Leucogranite, Mawat Ophiolite, northeastern Iraq:
723 Implications for Arabia–Eurasia continental collision. *Journal of Asian Earth Sciences*,
724 *Tectonics of Asia* 86:151–165.

725 Mohammad Y, Qaradaghi J (2016) Geochronological and mineral chemical constraints on the age and
726 formation conditions of the leucogranite in the Mawat ophiolite, Northeastern of Iraq: insight
727 to sync-subduction zone granite. *Arabian Journal of Geosciences* 9: 1-23.

728 Mohammad YO (2020) Cumulate and tectonite dunite from Mawat Ophiolite, Kurdistan Region,
729 Northeastern Iraq: Field evidence and mineral chemical constraints. *Iraqi*
730 *Bulletin of Geology and Mining* 16:15–33.

731 Mohammad YO, Ali SA, Aziz NR, Yar, IO, Abdulla KL (2021) Comment on “Generation and
732 exhumation of granitoid intrusions in the Penjween ophiolite complex, NW Zagros of the

733 Kurdistan region of Iraq: Implications for the geodynamic evolution of the Arabia-Eurasia
734 collision zone” by Ismail et al., 2020, V. 376–377, 105714. *Lithos* 390:105915.

735 Morgan, JJ (2005). Kinetics of reaction between O₂ and Mn (II) species in aqueous
736 solutions. *Geochimica et Cosmochimica Acta* 69: 35-48.

737 Mosier DL, Page N J (1988). Descriptive and Grade-Tonnage Models of Volcanogenic Manganese
738 Deposits in Oceanic Environments: A Modification (Vol. 1811, pp. 1-28). Washington,
739 United State of America, Government Printing Office.

740 Murray RW (1994) Chemical criteria to identify the depositional environment of chert: general
741 principles and applications. *Sedimentary Geology* 90:213–232.

742 Neff H (1994) RQ-Mode Principal Components Analysis of Ceramic Compositional Data.
743 *Archaeometry* 36:115–130.

744 Noda N, Imamura S, Sekine Y, Kurisu M, Fukushi K, Terada N, Uesugi S, Numako C, Takahashi Y,
745 Hartmann J (2019) Highly Oxidizing Aqueous Environments on Early Mars Inferred From
746 Scavenging Pattern of Trace Metals on Manganese Oxides. *Journal of Geophysical*
747 *Research:Planets* 124:1282–1295.

748 Nutman A, Ali S, Mohammad Y, Jones BG, Zhang Q (2022) The early Eocene (48 Ma) Qaladeza
749 trondhjemite formed by wet partial remelting of mafic crust in the arc-related Bulfat Igneous
750 Complex (Kurdistan, Iraq): constraints on the timing of Neotethys closure. *Arabian Journal*
751 *of Geosciences* 15: 679.

752 Oksuz N (2011) Geochemical characteristics of the Eymir (Sorgun-Yozgat) manganese deposit,
753 Turkey. *Journal of Rare Earths* 29:287–296.

754 Öztürk H (1997) Manganese deposits in Turkey: Distribution, types and tectonic setting. *Ore Geology*
755 *Reviews* 12:187–203.

756 Pirajno F (2009) Hydrothermal Processes Associated with Meteorite Impacts, in: Pirajno, F. (Ed.),
757 Hydrothermal Processes and Mineral Systems. Springer Netherlands, Dordrecht, 1097–1130.

758 Polgári M, Hein JR, VighT, Szabó-Drubina M, Főrizs I, Bíró L , Müller A, TóthAL (2012). Microbial
759 processes and the origin of the Úrkút manganese deposit, Hungary. *Ore Geology Reviews*, 47,
760 87-109.

761 Robertson AHF, Fleet AJ (1986) Geochemistry and palaeo-oceanography of metalliferous and pelagic
762 sediments from the Late Cretaceous Oman ophiolite. *Marine and Petroleum Geology* 3:315–
763 337.

764 Schlesinger WH, Bernhardt ES (2013) Biogeochemistry: an analysis of global change. Waltham, MA.

765 Sissakian V (2018) The Minerals Wealth in the Kurdistan Region, Iraq. *Journal of Science and*
766 *Engineering* 2:23–36.

767 Sun W, McDonough W (1989) Chemical and isotopic systematics of oceanic basalts: Implications for
768 mantle composition and processes, in: *Geological Society Special. Publication* 42: 313–345.

769 Taylor SR, McLennan SM (1985) *The Continental Crustal: Its Composition and Evolution*. Blackwell,
770 Oxford, UK, 312 pp.

771 Usui A, Nishimura A, Mita N (1993) Composition and growth history of surficial and buried
772 manganese nodules in the Penrhyn Basin, Southwestern Pacific. *Marine geology* 114:133–
773 153.

774 Usui A, Nishi K, Sato H, Nakasato Y, Thornton B, Kashiwabara T, Tokumaru A, Sakaguchi A,
775 Yamaoka K, Kato S (2017) Continuous growth of hydrogenetic ferromanganese crusts since
776 17 Myr ago on Takuyo-Daigo Seamount, NW Pacific, at water depths of 800–5500 m. *Ore*
777 *Geology Reviews* 87:71–87.

778 Xie C, Xu L, Peng, T, Chen K, Zhao J (2013) Leaching process and kinetics of manganese in low-
779 grade manganese ore. *Chinese Journal Geochemistry* 32:222–226.

780 Weast RC, Astle MJ (1986) Handbook of chemistry and physics CRC. Boca Raton, FL.

781 Yücel M, Gartman A, Chan CS, Luther III GW (2011) Hydrothermal vents as a kinetically stable
782 source of iron-sulphide-bearing nanoparticles to the ocean. *Nature Geoscience* 4: 367-371.

783 Zarasvandi A, Lentz D, Rezaei M, Pourkaseb H (2013) Genesis of the Nasirabad manganese
784 occurrence, Fars province, Iran: Geochemical evidences. *Geochemistry* 73:495–508.

785 Zarasvandi A, Rezaei M, Sadeghi M, Pourkaseb H, Sepahvand, M (2016) Rare-earth element
786 distribution and genesis of manganese ores associated with Tethyan ophiolites, Iran: A
787 review. *Mineralogical Magazine* 80:127–142.

788

